catalysts

MDPI

Article

Post Synthesis of Aluminum Modified Mesoporous TUD-1 Materials and Their Application for FCC Diesel Hydrodesulfurization Catalysts

Zesheng Xia [1,2], Jianye Fu [1], Aijun Duan [1,*], Longnian Han [2], Huadong Wu [3], Zhen Zhao [1,*], Chunming Xu [1], Dong Wang [2], Bo Wang [1] and Qian Meng [1]

1 State Key Laboratory of Heavy Oil Processing, China University of Petroleum, Beijing 102249, China; xzsb5291557@163.com (Z.X.); jianye.fu@uq.edu.au (J.F.); xcm@cup.edu.cn (C.X.); 18810418550@163.com (B.W.); d1732328127@163.com (Q.M.)

2 CNOOC Research Institute of Oil and Petrochemicals, Beijing 102209, China; hanln@cnooc.com.cn (L.H.); wangdong6@cnooc.com.cn (D.W.)

3 Key Laboratory of Green Chemical Process, Wuhan Institute of Technology (Ministry of Education), Wuhan 430073, China; wuhuadong@wit.edu.cn

* Correspondence: duanaijun@cup.edu.cn (A.D.); zhenzhao@cup.edu.cn (Z.Z.); Tel.: +86-10-8973-2290 (A.D.); +86-10-8973-1586 (Z.Z.)

Academic Editor: Adam F. Lee

Received: 22 February 2017; Accepted: 2 May 2017; Published: 7 May 2017

Abstract: Post-synthesis methods are a promising technology and have received much attention. In this paper, a series of post-synthesis aluminum modified TUD-1 (PAT) materials with different Al contents were successfully prepared by using aluminum isopropoxide to be Al sources, then the as-synthesized materials were adopted as support additives mixed with commercial γ-Al_2O_3 to prepare hydrodesulfurization (HDS) catalysts for FCC diesel. The supports and catalysts were analyzed using N_2 adsorption-desorption, XRD, SEM, Py-IR, ICP, ^{27}Al MAS NMR, UV-vis, H_2-TPR and HRTEM techniques. The results of Py-IR and ^{27}Al MAS NMR indicated that the addition of Al species could bring Lewis (L) and Brönsted (B) sites into Si-TUD-1, and that the material of PAT-3 had the highest total acidity sites and Brönsted acid sites among the series PAT composites. The HRTEM technique showed that, compared to the traditional catalyst NiMo/γ-Al_2O_3, the sulfided catalyst NiMo/APAT-3 had a relatively short length (3.2 nm) and suitable stacking number (2.5) of MoS_2 slabs. The HDS efficiencies of all the catalysts were tested in a fixed bed micro-reactor with FCC diesel as feedstock. The catalytic results confirmed that the catalyst NiMo/APAT-3 possessed the highest HDS efficiency (97.0%), due to synergistic effects of advantageous properties such as higher acidity, moderate MSI, and relatively short length of the MoS_2 slabs.

Keywords: aluminum modified; post synthesis method; TUD-1; FCC diesel

1. Introduction

Environmental protection is currently one of the hot topics, globally, so measures for solving air pollution are of significance and represent a great challenge for human beings. To this end, stringent environmental legislation impels the updating of fuel specification to higher levels; in particular, the sulfur content of transportation fuels is to be limited to lower than 10 ppm, and even to near 0 ppm in the near future [1]. Till now, hydrodesulfurization (HDS) has been the most widely applied technology for removing sulfur from fuels in modern refineries. The main purpose of HDS is to transform poor-quality diesel into an ultraclean final product, while the keypoint is the novel HDS catalyst. However, traditional Al_2O_3 support used in commercial hydrotreating catalysts cannot completely achieve ultra-deep HDS due to its single L acid site, amorphous pore structures, and

strong metal-support interaction (MSI) over alumina support [2,3]. Alternative methods include improving the acidity and pore structure of the supports by introducing acidic porous materials into the catalyst system. Furthermore, the synergistic effects of B and L acid sites are essential to HDS, hydroisomerization and hydrodearomatization reactions [2,3]. Thus, the development and synthesis of novel acidic catalytic materials with low cost will be an important aspect of realizing the production of ultra-clean diesel.

In terms of HDS catalysts, their supports generally require open and interconnected pore structures to eliminate the steric effect of refractory reactants like 4,6-dimethyldibenzothiophene (4,6-DMDBT), and also require a suitable acid property for the desulfurization reactions to take place.

Since the discovery of M41S mesoporous silicas, symbolizing a significant finding in the material synthesis field, mesoporous materials have aroused much more attention in terms of their synthesis, modification and application. However, pure silica has an electrically neutral framework and therefore expresses no acid sites, resulting in a relatively weak acid catalytic reaction [4]. Recently, many studies have been devoted to the incorporation of Al, Ti, Zr, Sn and V species into the framework of SBA-15 for modulating redox and acidity properties [5]. Typical methods have included "post synthesis" [4,6,7] and "direct synthesis" [8,9] grafting procedures. Direct synthesis methods incorporate aluminum species into the original synthesis system before hydrothermal processing under specialized conditions; however, the respective structures of the materials and the structure order are usually destroyed as the metal content increases. Therefore, some previous studies [4,10–12] have reported that Al could be effectively incorporated into silicas via various post-synthesis processes with anhydrous $AlCl_3$ [10], aluminum isopropoxide [11] or with sodium aluminate [12] followed by calcination. The incorporated alumina in the tetrahedral framework are associated with the presence of accessible hydroxyl groups in a silica matrix, bringing more acid sites to the molecular sieve, which then influence the catalytic properties of the materials [4,13].

Mokaya et al. [11] proved that Al-containing MCM-41 in good order could be synthesized using a post-synthesis method by grafting Al-alkoxide with siliceous MCM-41 in nonaqueous media. They found that the final materials retained the hexagonal pore structure and characteristics of the parent material MCM-41, and exhibited higher Brönsted acid amounts compared with the counterpart Al-MCM-41 produced by conventional direct-synthesis methods. The authors attributed the higher acid contents to the existence of B acid generation from Al species.

Luan et al. [4] synthesized SBA-15 material and incorporated it with Al species to obtain Al-SBA-15 via three different post-synthesis routes by reacting SBA-15 with different Al resources, including $AlCl_3$, aluminum isopropoxide and sodium aluminate. The characterization results showed that the Si/Al ratios in the final products were in accordance with the compositions in the post-synthesis mixtures, indicating the fact that alumina were mostly implanted into the silica SBA-15 materials in a range of Si/Al = 10–40.

Suresh et al. [14] reported systematic research of sulfided Mo-Ni catalysts over Al-SBA-15 through a post-synthetic method. The catalytic results showed that the improved hydro-denitrogenation activity on the aluminum incorporated catalysts could be mainly ascribed to the substitution of Al, causing the formation of active phases.

The high expense of the surfactants in the synthesis of mesoporous materials impedes wide application in industrial production; meanwhile, the development of low-cost catalysts favors large-scale manufacturing processes [15]. Based on the above strategy, there has been an increasing taste for the application of "surfactant-free" methods of synthesizing mesoporous materials (such as silica, titania and aluminiumphosphate (ALPOs)) by using small, low-cost organic molecules (e.g., citric acid, urea, tartaric acid or cyclodextrins, among others) [16–20].

In 2001, purely siliceous TUD-1 was first published by Jansen et al. [21]. It was synthesized using a cost-effective synthesis (surfactant-free) method using triethanolamine (TEA) as a template. TUD-1 possesses many advantages compared to other mesoporous materials, such as high surface

area, sponge-like interconnecting porous structures, good basement accessibility and tunable pore size distribution [22,23], all of which make it a potential support additive for HDS catalysts.

Owing to the good performance of Al incorporated into supports through post-synthetic methods, and the advantages of the material TUD-1, a series of PAT materials with different Al contents produced via a post-synthetic alumination procedure were successfully synthesized by using aluminum isopropoxide in organic solvents as the Al source. Then the as-synthesized materials were adopted as support additives, and mixed with the commercial γ-Al_2O_3 through a mechanical grinding method to prepare the HDS catalyst for FCC diesel hydrotreating. The supported catalysts were prepared using Ni and Mo as the active metals. The as-synthesized supports and the corresponding NiMo catalysts were analyzed using N_2 adsorption-desorption, XRD, SEM, Py-IR, ^{27}Al MAS NMR, UV-vis, H_2-TPR ICP and HRTEM methods. The catalytic performances of all catalysts were tested with FCC diesel fuel as feedstock. The correlation between the HDS activities and the physicochemical properties of the catalysts were analyzed systematically. Compared with other catalysts, the catalyst NiMo/APAT-3 had the highest HDS efficiency (97.0%).

2. Results

2.1. Characterization Results of the Support Additives

2.1.1. XRD Characterization of Support Additives

From low-angle XRD patterns as shown in Figure 1a, the XRD analyses of PAT materials are the same as those for the parent purely siliceous TUD-1, showing only one typical peak (from 0.5–2° in 2θ) [22], meaning the mesoporous structure is maintained.

In the wide-angle domain, from Figure 1b, all mesoporous metallosilicates obtained by the post-synthetic grafting method show similar XRD patterns to their parent silica materials, with only a very broad peak centered around 2θ of 24° assigned to the amorphous silica [24]. Meanwhile, no characteristic reflections associated with γ-Al_2O_3 are detected, meaning that no bulky γ-Al_2O_3 aggregates exist, and that the coated metal species are well distributed on the external surface, and are probably implanted within the silica framework after calcination.

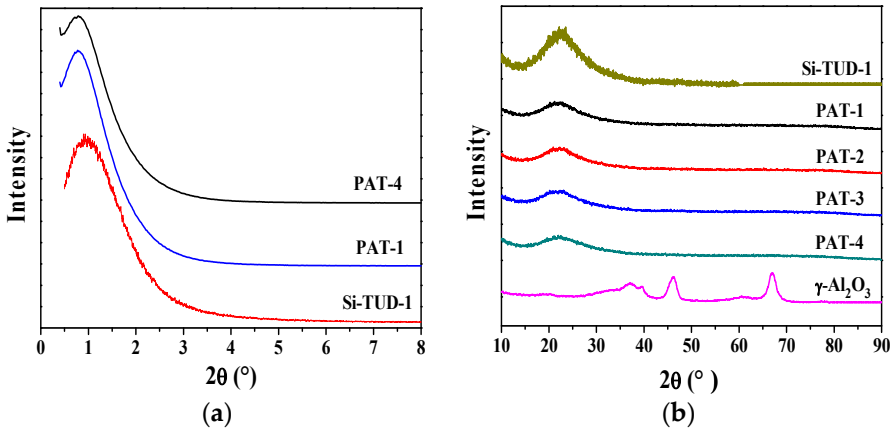

Figure 1. X-ray diffraction (XRD) patterns (**a**) low-angle patterns; (**b**) wide-angle patterns.

2.1.2. N_2 Adsorption-Desorption of Support Additives

As shown in Figure 2, the PAT samples and pure Si-TUD-1 show "type IV" adsorption isotherms (Figure 2a) according to the IUPAC classification, and narrow pore-size distributions (Figure 2b) [25–27], meaning that these materials have a mesoporous structure and the original mesostructure of Si-TUD-1 is well retained after Al incorporation by post-synthesis methods. The hysteresis loops of all the samples are similar to type H_2, which signifies the presence of non-negligible secondary mesoporous

materials. The changes of N_2 adsorption contents at P/P_0 = 0.4–0.8 verify the presence of network effects. In particular, the absence of transformation at about P/P_0 = 0.4 signifies the feasibility of pore blocking [28]. The four PAT series materials all have the same type IV isotherms, demonstrating that the post-synthesis alumination method can retain the mesoporous structure of TUD-1.

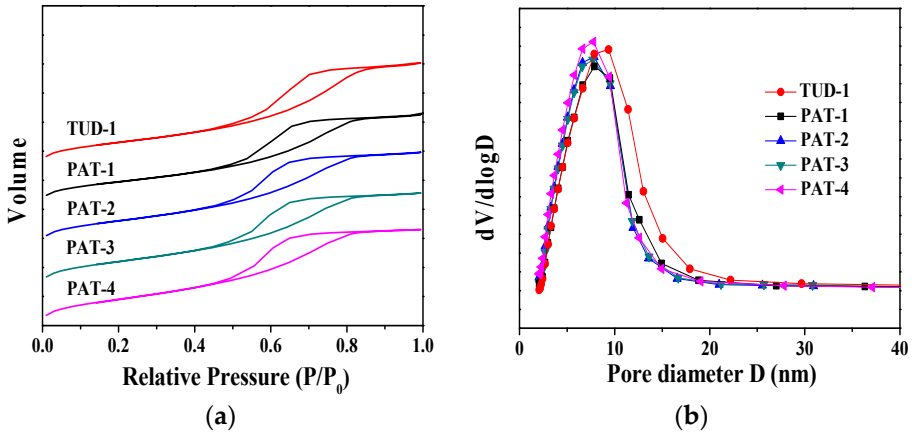

Figure 2. The N_2 adsorption-desorption isotherms (**a**) and pore diameter distributions (**b**).

Table 1 shows the results for the surface area calculated from the absorption branch, while volume and diameter are calculated from the adsorption branch. From Table 1, it is obvious that with the increase of Al content, surface area shows a continuous decreasing tendency. The same is true for volume and diameter (with a range from 0.66 to 0.55 $cm^3\ g^{-1}$, and 6.6 to 5.5 nm, respectively), which may be attributable to an increase in wall thickness after the deposition of Al. It may be concluded that, with the increase of Al during the post-synthesis method, parts of alumina species will attach to the mesopore wall or block the channel hole, resulting in a slight reduction in the sizes of channels and the volumes of mesopores. It also can be found that the pore diameter of commercial γ-Al_2O_3 is the largest, reaching 12.5 nm, while the surface area is the lowest.

Table 1. Textural characteristics of commercial γ-Al_2O_3 and the support additives.

Material (%Al_2O_3)	S_{BET} ($m^2\ g^{-1}$)	V_{BJH} ($cm^3\ g^{-1}$)	D (nm)
γ-Al_2O_3	189.7	0.67	12.5
Si-TUD-1 (0)	420.7	0.66	6.6
PAT-1 (3%)	389.8	0.60	6.4
PAT-2 (6%)	390.9	0.58	6.0
PAT-3 (12%)	381.6	0.57	5.6
PAT-4 (18%)	342.3	0.55	5.5

2.1.3. SEM and EDX Characterizations of the Support Additives

To further study the surface morphology of the PAT series materials, the SEM technique was adopted, and the images are shown in Figure 3. The micrographs of PAT-1, PAT-2, PAT-3 and PAT-4 are analogous to the pure TUD-1, with irregular morphology as reported by other research [29].

The irregular surface structure of the sample is formed by the random packing of solid particles into sporadic, amorphous shapes, and the particle sizes range mainly from nanometer to micrometer size. It can also be seen that with the increase of Al (from Figure 3A–D), the volume of bulk particles packed on the surface increases; a possible reason being that parts of the aluminum species weren't implanted into the skeleton of the purely siliceous TUD-1 in the post-synthetic process, which is in accordance with the results of ^{27}Al MAS NMR in Figure 6. Therefore, these alumina attach to the material surfaces, leading to the disordered morphology generated by particle accumulation.

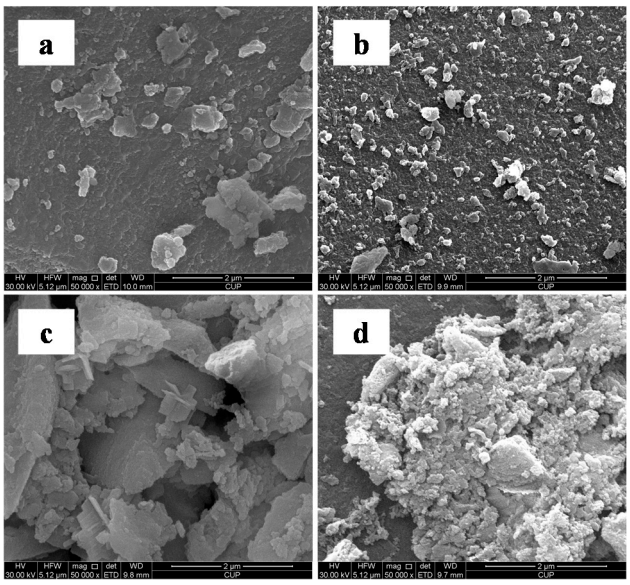

Figure 3. Scanning electron microscopy (SEM) characterizations of the support additives. (**a**) PAT-1; (**b**) PAT-2; (**c**) PAT-3; (**d**) PAT-4.

The elemental analysis is confirmed by energy-dispersive X-ray spectrometer (EDX) technique, as shown in Figure 4. From EDX characterizations, the presence of Al elements on the surface is obvious. The EDX microanalyses also confirm that aluminum elements are homogenously distributed throughout the PAT series materials, in accordance with the results of EDS elemental mapping technology exhibited in Figure S1 in the Supplementary Information section. The inserted squares in Figure 4A–D represent the analysis positions, which show that the Al species content (the given values correspond to the EDX analysis as shown in Table 2) of the PAT series materials is less than in the corresponding original systems, confirming that not all Al elements introduced in the post-synthesis system were implanted into the framework of the final products. This could be explained by the fact that parts of aluminum species are washed away during the filtration and washing processes in the post-synthetic procedure. Table 2 lists the utilization ratios of alumina in the post synthesis modification process. From Table 2, it is obvious that the Si/Al proportions obtained by the two analysis techniques of every Al-grafted sample are similar, illustrating that the majority of Al has a homogenous distribution throughout the PAT materials, and that the post-synthesis grafting method has good potential utility in incorporating discrete amounts of metal heteroatoms into the purely siliceous material of Si-TUD-1. It also can be seen that with the increase of Al, the aluminum content in the final product increases, and the aluminum utilization ratios increase at first, and subsequently decrease, while the PAT-2 has the highest aluminum utilization rate (60.6%).

Table 2. The utilization ratios of alumina in the post synthesis modification process.

Material	Al_2O_3 (wt %) [1]	Product Si/Al	Utilization Ratio
PAT-1	3%	67 [2] (65.6) [3]	59.7%
PAT-2	6%	33 (32.2)	60.6%
PAT-3	12%	17 (17.0)	58.8%
PAT-4	18%	9 (8.5)	55.6%

Note: [1] the Al_2O_3 percentage of the alkoxide addition amounts in the post synthesis method; [2] the given values out of parenthesis are corresponding to the EDX analysis; [3] the values shown in parenthesis are obtained from ICP analysis.

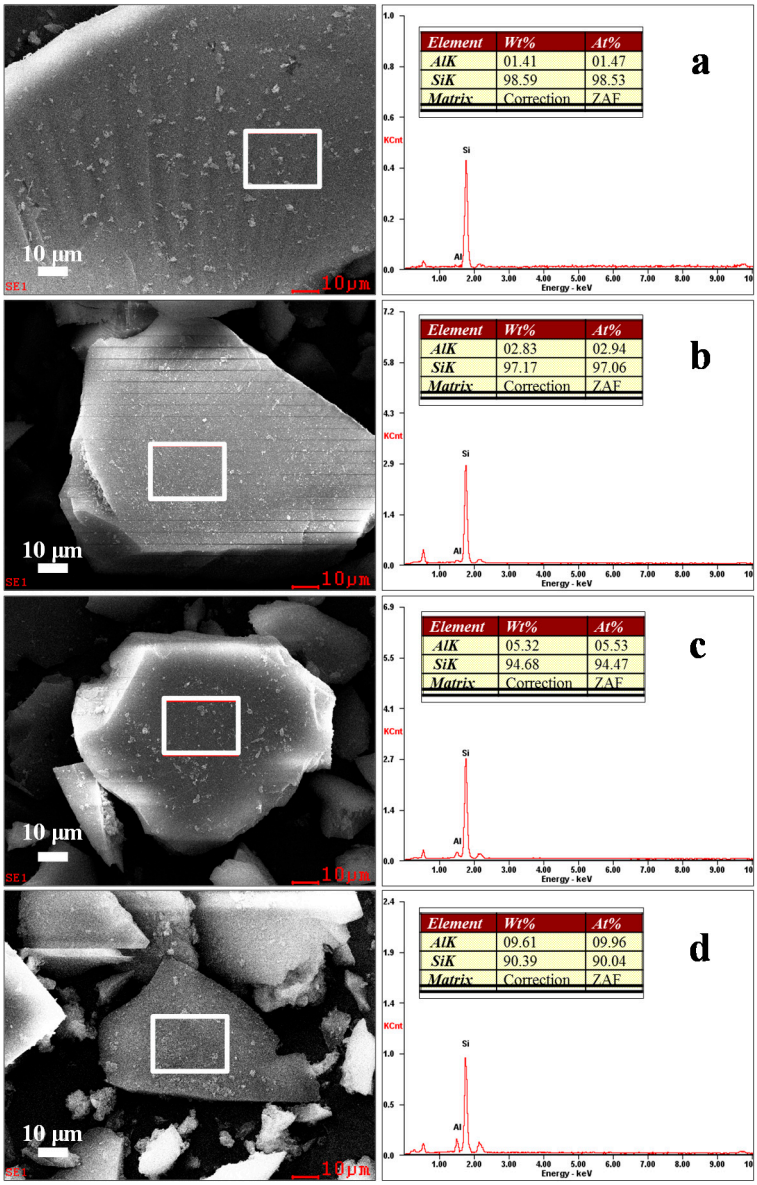

Figure 4. EDX characterizations of the support additives. (**a**) PAT-1; (**b**) PAT-2; (**c**) PAT-3; (**d**) PAT-4.

2.1.4. Py-IR Characterization of the Support Additives

The types and distribution of acid sites brought by the incorporation of Al elements of the PAT series materials and their counterparts, aluminum in-situ modified TUD-1 (Al-TUD-1) and the purely siliceous TUD-1, are investigated by the FT-IR method, and the results are exhibited in Figure 5A,B. According to the literature [30,31], the bands at 1540 and 1450 cm^{-1} are attributed to B and L acid sites, respectively, whereas the band at 1490 cm^{-1} is assigned to adsorbed pyridine bonded to both the L and B sites. The total amounts of weak acid sites and that of medium and strong sites are detected by the FT-IR method after degassing at 473 K and 623 K, respectively.

Detailed data about B and L sites and the ratios of B/L are shown in Table 3. Obviously, the incorporation of Al elements into the pure TUD-1 has an effect on the acidic properties, whereby Si-TUD-1 has no acid sites, and the acidic properties of the PAT series materials are enhanced to the same level as Al-TUD-1; from which it can be concluded that the grafting operation of Al alkoxide in organic solvents on Si-TUD-1 can modify the surface properties of the silica material, just like the conventional direct synthesis method. After degassing at 473 K, with the increase in Al content, the

amounts of L acid sites have a decrease tendency and the B sites increase first, then decrease, but the total contents of B + L sites and the ratio of B/L of PAT-3 reach the highest. After degassing at 623 K, no B sites are observed in the Py-IR profiles of PAT-1 and PAT-2, while the medium and strong acid site numbers are highest for PAT-3. Compared with PAT-3, the B sites and total acid sites of the PAT-4 material has a slight reduction, which can be attributed to the fact that excessive Al species cover the internal surface and external surface of PAT materials, constructing extra-framework aluminum, as can be seen from the SEM images. This suggests that appropriate amounts of Al species can bring about the desired Brönsted acid and total acidity.

Thus, the as-prepared PAT series materials possessed both B and L acidities originated from the incorporation of Al into the purely siliceous TUD-1 materials, therefore facilitate to the HDS performance of the catalysts.

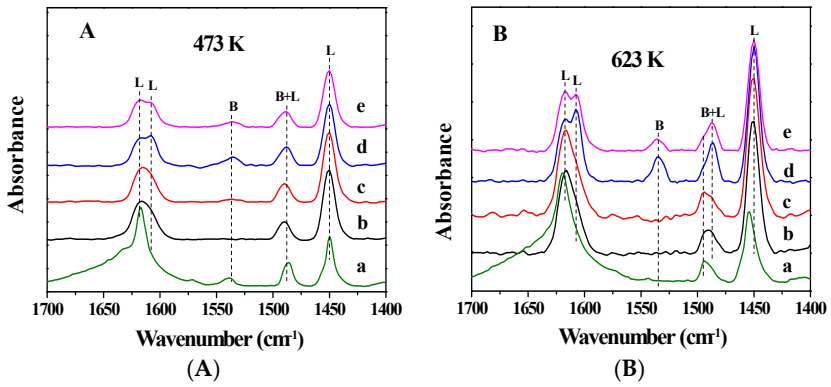

Figure 5. The Py-IR profiles of the support additives after degassing at (**A**) 473 K and (**B**) 623 K. (a) Al-TUD-1, (b) PAT-1, (c) PAT-2, (d) PAT-3, (e) PAT-4.

Table 3. The amounts of B and L acid analyzed by Py-IR of the support additives.

Material	473 K Acid Sites (μmol g^{-1})				623 K Acid Sites (μmol g^{-1})			
	L	B	L + B	B/L	L	B	L + B	B/L
Si-TUD-1	0	0	0	–	0	0	0	–
Al-TUD-1	58.0	13.2	71.2	0.23	58.0	0	58.0	0
PAT-1	70.8	3.5	70.8	0	35.6	0	35.6	0
PAT-2	72.5	5.5	78.0	0.08	36.4	0	36.4	0
PAT-3	59.7	19.6	79.3	0.31	30.7	7.9	38.6	0.26
PAT-4	54.0	9.7	63.7	0.18	25.3	3.5	28.8	0.14

2.1.5. ^{27}Al MAS NMR Spectra of the Support Additives

To investigate the coordination states of aluminum species with the TUD-1 framework, ^{27}Al MAS NMR analyses of calcined PAT series samples and Al-TUD-1 were analyzed. Shown in Figure 6, and similar to the spectra of Al-TUD-1, three peaks can also be found for the calcined PAT series materials, representing the fact that the calcined PAT series materials and Al-TUD-1 have the same types of Al species. And the different intensity order of the peak means different proportions of Al species in each sample. The peak near 0 ppm can be attributed to hexacoordinated Al (structural unit AlO_6), indicating the existence of non-framework Al on the parent TUD-1. The peak at δ = 58 ppm can be ascribed to tetracoordinated Al (structural unit AlO_4), and is generally related to the desired B sites (Si-O(H)-Al) [32], suggesting parts of Al implanted into the silica framework. Besides these two main peaks, the third signal is around δ = 34 ppm, the peak could be related to Al in a pentahedral coordination (structural unit AlO_5), possibly situated in the interface between the aluminosilicate and the amorphous Al phases [33]. The chemical shift of the tetra-coordinated Al at δ = 58 is less than that of bulk γ-Al_2O_3 (the peak at δ = 65 ppm), indicating the existence of Al-O-Si bonds due to the Al

elements implanted into the framework [34,35]. The peak at δ = 30 ppm explains the presence of an amorphous alumina phase [36]. From Figure 6, it can be seen that the intensity of the pentacoordinated Al increases with the increase of Al in the alumination process from the materials of PAT-1 to PAT-4, which means that a pure material TUD-1 can be gradually modified in its physicochemical properties by grafting Al species onto its surfaces [36,37]. This might be explained by the SEM results, in which the volume of bulk particles packed onto the surface increases with the increase of aluminum content in the synthesis process. As is well known, pure silica or alumina material don't have B sites, so appropriate amounts of Al species grafted to the pure silica material will be favorable to the generation of Brönsted acid sites, which is confirmed by the results of Py-IR characterization. Morevoer, the existence of tetrahedral Al is clear evidence that parts of Al atoms are implanted into the siliceous skeleton of TUD-1 analogous to the assembly of Al-TUD-1.

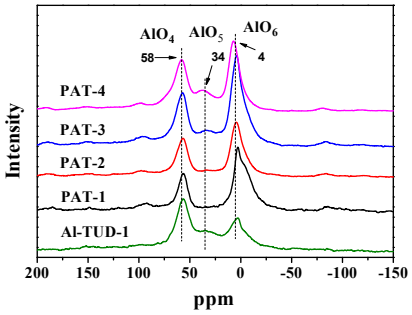

Figure 6. ^{27}Al MAS NMR spectra of the support additives.

2.2. Characterization Results of the Corresponding Catalysts

2.2.1. XRD Characterization of the Corresponding Catalysts

Figure 7 is the wide XRD of the supported catalysts. It could be seen that the intensity of characteristic peaks of γ-Al_2O_3 decreases after the loading of active metals and all catalysts have strong peaks at 37.60, 45.84 and 67.30 in curves (a–e), which are assigned to γ-Al_2O_3 [38,39]. And weak XRD diffraction peaks at 2θ = 27.3 belong to MoO_3; whereas there is no diffraction peak correlated to NiO or $NiAl_2O_4$ crystal phases, demonstrating that the Ni elements are relatively well scattered on the surface. Compared with NiMo/γ-Al_2O_3, the series catalysts of NiMo/APAT-x appear to have a weak diffraction peak of MoO_3, suggesting that a small number of MoO_3 crystallines are present on the supports, and the MSI in the PAT materials used as the support additives aren't as strong as that of the γ-Al_2O_3 supported catalyst. However, the well scattered MoO_3 nanocrystalline phases with suitable stacks are conducive to the generation of "type II" active phases, which could produce sufficient brim and edge sites for the HDS reaction [40], while the weak MSI facilitates the generation of small piled MoO_3 crystals.

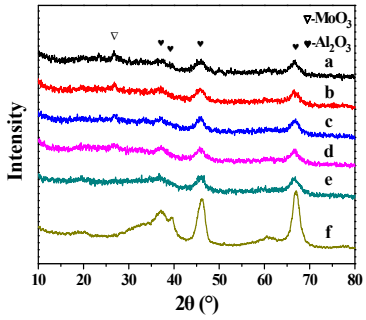

Figure 7. XRD patterns of the corresponding catalysts. (a) NiMo/APAT-1, (b) NiMo/APAT-2, (c) NiMo/APAT-3, (d) NiMo/APAT-4, (e) NiMo/γ-Al_2O_3, (f) γ-Al_2O_3.

2.2.2. N_2 Adsorption-Desorption of the Corresponding Catalysts

As shown in Figure 8, the textural properties of NiMo supported series catalysts exhibit typical type IV adsorption isotherms and H_2 hysteresis loops (Figure 8a), suggesting the existence of mesoporous structures and narrow pore-size (Figure 8b) [25–27]. Table 4 is the sum of the surface areas and other textural properties of the catalysts.

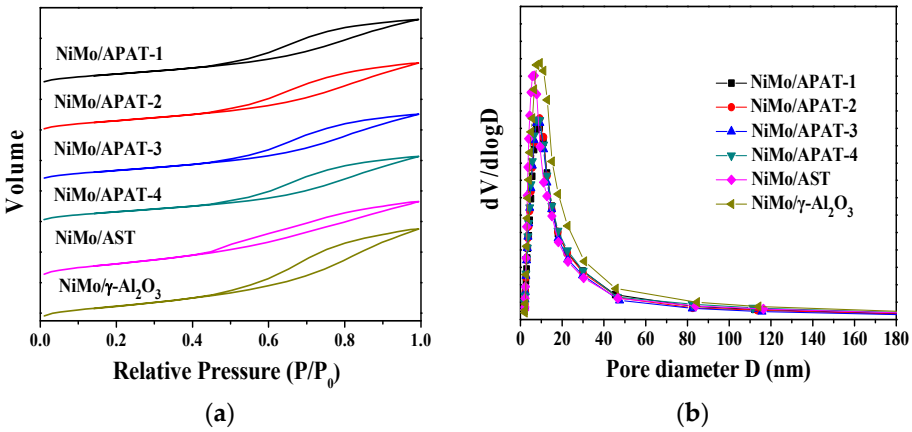

Figure 8. The N_2 adsorption-desorption isotherms (**a**) and pore size distributions (**b**).

Table 4. Textural characteristics of the different catalysts.

Catalyst	S_{BET} (m^2 g^{-1})	V_{BJH} (cm^3 g^{-1})	Pore Diameter (nm)
NiMo/AST	283.0	0.47	6.6
NiMo/APAT-1	236.7	0.41	7.3
NiMo/APAT-2	227.4	0.39	7.5
NiMo/APAT-3	225.6	0.40	7.3
NiMo/APAT-4	224.2	0.39	7.1
NiMo/γ-Al_2O_3	167.4	0.34	8.3

From Table 4, it can be seen that the surface area and pore volume of NiMo/AST catalysts are higher than those of NiMo/APAT-x series catalysts, and the catalyst of NiMo/γ-Al_2O_3 had the smallest surface area and pore volumes. However, the pore diameter had a contrary tendency of these catalysts. The surface areas of the catalysts of NiMo/APAT-x series are around 220 m^2 g^{-1}, and the diameters are estimated around 7 nm. Among the series catalysts of NiMo/APAT-x, the catalyst of NiMo/APAT-4 has the smallest surface area, volume and diameter. Compared with the textural properties of the materials in Table 1, the surface area and volume diminish under different degrees after the loading of active metal components, which may be attributed to pore blockage caused by metal oxides during the impregnation process. As is known to all, large surface area is proper for good distribution of metals, while large diameter facilitates the elimination of diffusion resistance.

2.2.3. UV-Vis Spectra of the Corresponding Catalysts

UV-is adopted to characterize the local structures concerning the coordination states of Mo species on the supports. Accordingly, the adsorption bands are produced by the ligand-to-metal charge transfer, O^{2-} to Mo^{6+} [41,42]. The band positions are determined by the Mo species coordination and agglomeration degrees in the samples. Figure 9 exhibits the UV-vis of the NiMo/APAT-x series catalysts. According to [43], the absorption band from 220 to 250 nm is generally assigned to molybdate in isolated tetrahedral coordination, and the band from 260 to 320 nm is attributed to the octahedral coordination, while the bulk MoO_3 absorption peak is between 340 and 390 nm. The spectra apparently show that the band region of Mo oxide species changes with different amounts of aluminum in the

catalysts. The characteristic region of Mo(Oh) (between 260 and 320 nm) widens with increasing aluminum amounts, which suggests that the grafting of Al atoms into the Si-TUD-1 material is conducive to forming octahedral coordination of Mo species, which is confirmed by the result for H_2-TPR. These octahedral coordinations are more likely to produce the sulfur vacancies, favorable for improving the catalytic performances of the HDS reaction [44]. In addition, no obvious peaks of NiO and $NiMoO_4$ are discovered at around 330–350 nm or 725–740 nm, implying good dispersion of Ni and Mo species.

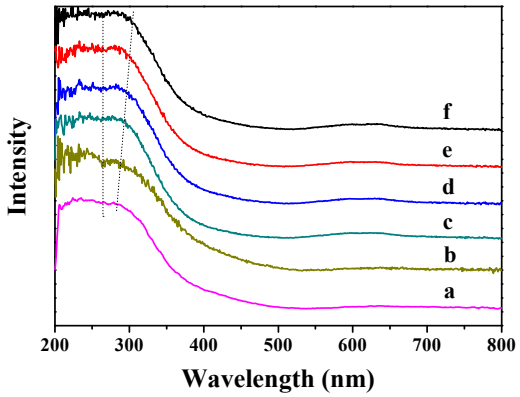

Figure 9. UV-vis spectra of the corresponding catalysts. (a) NiMo/γ-Al_2O_3, (b) NiMo/AST, (c) NiMo/APAT-1, (d) NiMo/APAT-2, (e) NiMo/APAT-3, (f) NiMo/APAT-4.

2.2.4. H_2-TPR Characterization of the Corresponding Catalysts

To more closely examine the redox characteristics and the MSI, H_2-TPR characterizations were carried out, and the profiles are shown in Figure 10. The H_2-TPR curves of the materials show two apparent reduction peaks at 673–753 K and 1043–1173 K, respectively. The low reduction peak at around to 743 K is generally attributed to the first step reduction of highly-dispersed polymeric octahedral Mo species (Mo^{+6} to Mo^{+4}), considered to be the precursors of "type II" active phases (Ni-Mo-S) [45–47]. The other peak at around 1073 K is associated with the deep reduction (Mo^{+4} to Mo^0) of all Mo species, including tetrahedral Mo elements, bulk crystalline MoO_3 or $Al_2(MoO_4)_3$ [48]. However, no apparent reduction peaks ascribed to large MoO_3 particles are observed in any of the catalysts within the temperature range of 873–903 K, suggesting that the Mo elements are well scattered on the supports; moreover, these results are confirmed by the XRD characterization results. Compared to NiMo/γ-Al_2O_3, which shows two main reduction peaks at 750 and 1142 K; the NiMo/APAT-x series catalysts, which show two obvious TPR peaks, shift to a lower temperature, indicating the combination of γ-Al_2O_3 and PAT series materials, causing the reduction of Mo species on the supported catalyst more easily than for γ-Al_2O_3, which can be ascribed to the reasonable MSI. These are in accord with the XRD characterization of the catalysts, since the MSI in the PAT materials is lower than that in the γ-Al_2O_3 supported catalyst. From the curves b to e in Figure 10, the low reduction peak of Mo species shifts to a slightly higher temperature, with a range from 716 to 722 K, which indicates that more Al species result in stronger MSI. The H_2-TPR patterns change due to the formation of some Mo species that are more easily reduced with the increase in Al amounts in the samples, which is in agreement with the UV-vis spectra result. The catalyst of NiMo/γ-Al_2O_3 usually has a stronger MSI than those of NiMo/APAT-x, leading to the generation of "type I" Ni-Mo-S phases with a comparatively inferior HDS efficiency.

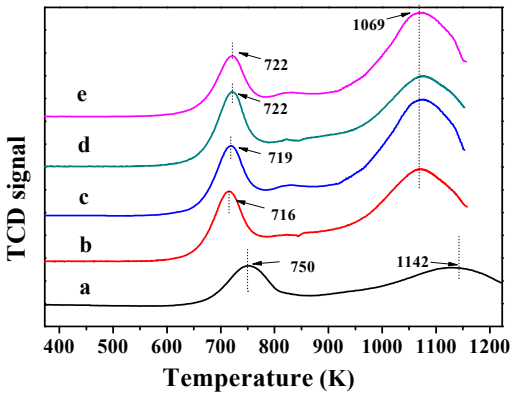

Figure 10. H_2-TPR profiles of the corresponding catalysts. (a) NiMo/γ-Al_2O_3, (b) NiMo/APAT-1, (c) NiMo/APAT-2, (d) NiMo/APAT-3, (e) NiMo/APAT-4.

2.2.5. HRTEM of the Corresponding Sulfided Catalysts

The HRTEM technique was applied to visualize the morphology of the active phases of the MoS_2 crystallite slabs over these catalysts. In Figure 11, the representative images of the sulfided catalysts with the layer number distributions and the length distributions of MoS_2 slabs are displayed. The results of the average length and layer number of MoS_2 crystallites, which were measured through the statistical analysis of about 25 representative images including over 300 slabs obtained from each catalyst, are shown in Table 5. The average length (L_{av}) and layer number (N_{av}) were obtained from the following Equation (1) [49]:

$$L_{av}(N_{av}) = \sum_{i=1}^{n} xiM_i / \sum_{i=1}^{n} xi \quad (1)$$

where M_i is denoted as the length or the layer number of a MoS_2 unit, and x_i is the number in a given scale of length or layer. The f_{Mo} parameter, which represents the dispersion degree of edge Mo atoms, is calculated according to Equation (2) [50,51]:

$$f_{Mo} = \sum_{i=1}^{t}(6ni - 6) / \sum_{i=1}^{t}(3ni^2 - 3ni + 1) \quad (2)$$

t is the total number and ni is the number of edge Mo atoms calculated from the length (L = 3.2 $(2ni - 1)$ Å) obtained by HRTEM.

The Ni-Mo-S model has been widely applied in the measurement of catalytic properties. Depending on the nature of MSI, the model of Ni-Mo-S structure can present two different types ("type I" or "type II") [52]. "Type I" has a low intrinsic activity due to the strong MSI and "type II" has an enhanced intrinsic activity with more accessible edge and corner sites due to the reasonable MSI. Appropriate MSI is beneficial for increasing the sulfidation of Mo oxide and producing active sites favorable for the HDS reaction [53].

In Figure 11C, the MoS_2 slabs of NiMo/γ-Al_2O_3 sulfided catalyst is less stacked with layer number 1 or 2, which can be associated to the intensely acting force between Mo and hydroxyl groups, resulting in the relatively low sulfided Mo species, and therefore show lower activity. From Figure 11A,B, the layer number of MoS_2 slabs are higher with the most layer numbers concentrated on two or three layers. Compared with the sulfided NiMo/γ-Al_2O_3 catalyst, the catalysts doped with the material TUD-1 modified by post or direct synthetic alumination procedure show relatively short lengths of the MoS_2 slabs as shown in Figure 11D. A suitable dispersion of the active phase is essential for the formation of accessible active centers. Short length and suitable stacking of the MoS_2 slabs facilitate the generation of more "type II" phases [13]. The results in Table 5 suggest that the lengths and stacking number of MoS_2 slabs change with different catalyst supports. It can also be seen from Table 5 that the NiMo/γ-Al_2O_3 sulfided catalyst has the longest length (3.9 nm) and lowest stacking

number (1.6) of all of the MoS_2 slabs due to the strong MSI, consistent with the XRD and H_2-TPR results, which implies that the state of most active sites is "type I". In comparison with the sulfided NiMo/γ-Al_2O_3 catalyst, the two catalysts of NiMo/AAT and NiMo/APAT-3 show relatively short lengths and suitable layer MoS_2 slabs, which suggests that the majority of active sites are in "type II" phases. This is in accordance with the fact that the incorporation of Al elements results in a reasonable MSI, confirmed by the H_2-TPR results. Moreover, the catalysts of NiMo/AAT and NiMo/APAT-3 are with f_{Mo} values of 0.32 and 0.31 respectively, and these f_{Mo} values are significantly higher than the traditional NiMo/γ-Al_2O_3 catalyst, confirming that the catalyst NiMo/γ-Al_2O_3 possesses lower active edge sites.

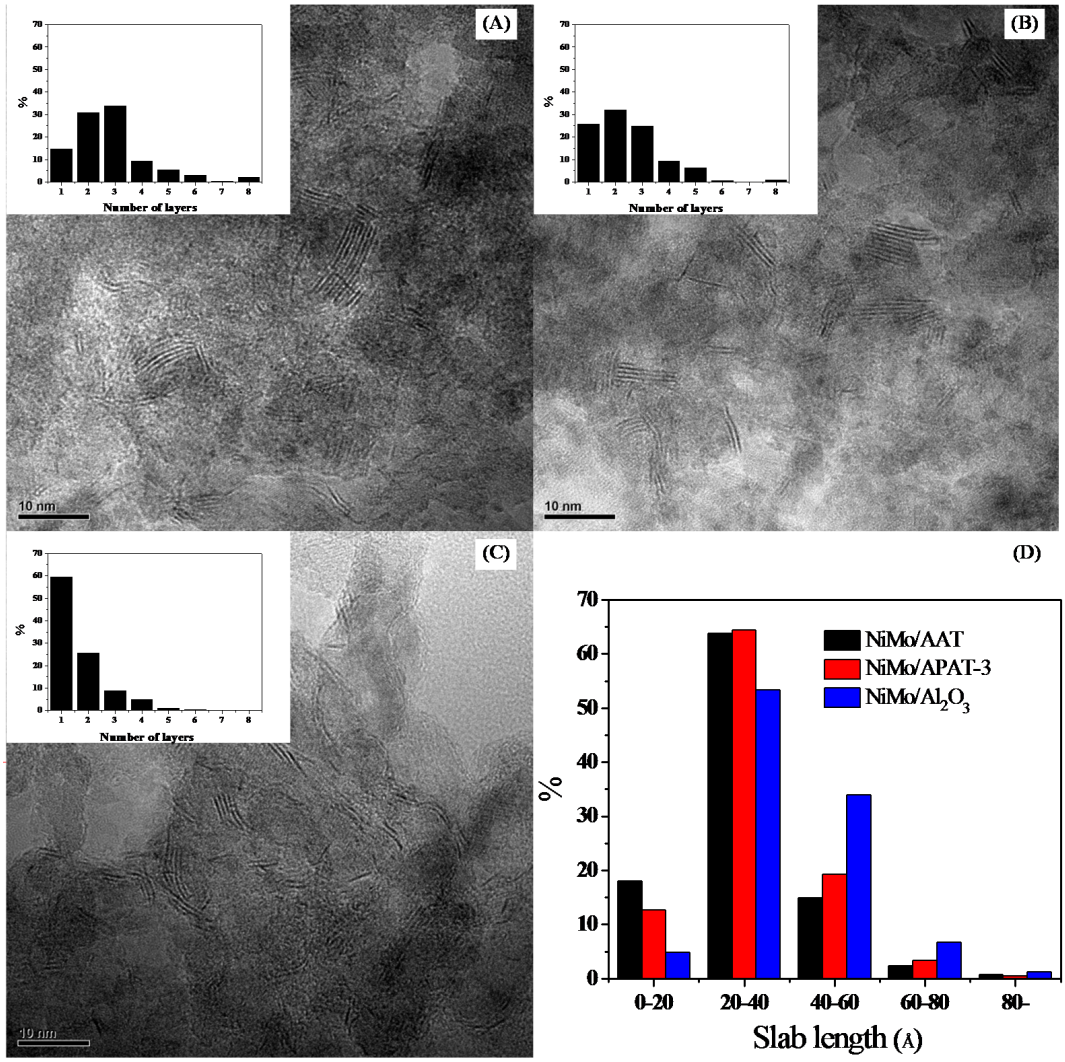

Figure 11. HRTEM micrographs of the corresponding catalysts. (**A**) NiMo/AAT; (**B**) NiMo/APAT-3; (**C**) NiMo/γ-Al_2O_3; (**D**) the distribution of length in Å of the MoS_2 particles.

Table 5. Average length (L_{av}) and layer number (N_{av}) of MoS_2 crystallites.

Catalyst	L_{av} (nm)	N_{av}	f_{Mo}
NiMo/AAT	3.0	2.8	0.32
NiMo/APAT-3	3.2	2.5	0.31
NiMo/γ-Al_2O_3	3.9	1.6	0.26

It is important to notice that the exposure brim sites of the top layer of multi-stacks favor hydrogenation reactions, which means that if the layer number of the MoS_2 slabs is too high, the accessible active sites will reduce in reverse. According to the results displayed in Table 5, the catalyst of NiMo/APAT-3 could enhance HDS activities than the catalysts of NiMo/AAT and NiMo/γ-Al_2O_3.

2.3. HDS Efficiency of FCC Diesel

In this paper, HDS catalytic activities of NiMo/APAT-x series catalysts using PAT series materials as the support additives with different Al contents were evaluated in a microreactor plant using FCC diesel oil as feedstock, while the NiMo/γ-Al_2O_3, NiMo/AAT and NiMo/AST catalysts were used as reference for comparison.

As can be seen in Figure 12 and in Table 6, compared with the catalyst NiMo/γ-Al_2O_3, the catalysts containing PAT additives showed higher HDS conversions, and among these catalysts NiMo/APAT-3 showed the highest HDS efficiency (97.0%). For the series catalysts of NiMo/AST and NiMo/APAT-1 to NiMo/APAT-4, along with the increased amount of Al, the efficiencies increased at first and reached a maximum of 97.0% when the Al to Si ratio was equal to 17, then slightly decreased to 96.5% as Si/Al = 9. It can also be observed that the catalyst NiMo/AAT had a HDS efficiency of 96.6%. The overall catalytic performance of FCC diesel over different catalysts is associated with the synergistic effects of physicochemical characteristics of the catalysts.

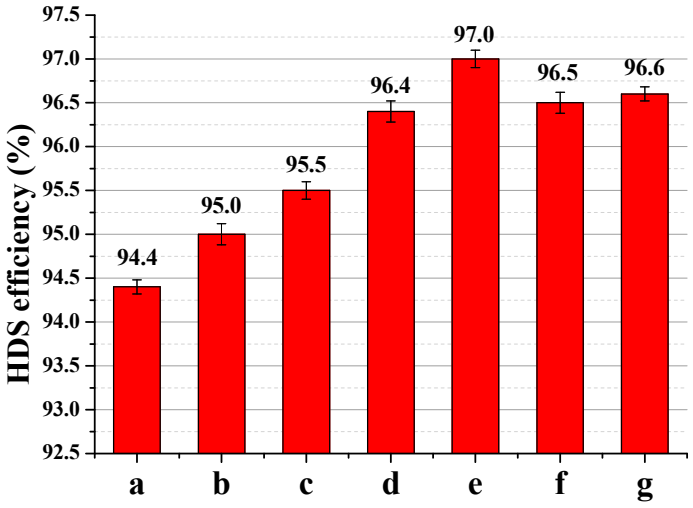

Figure 12. HDS efficiency of the corresponding catalysts. (a) NiMo/γ-Al_2O_3, (b) NiMo/AST, (c) NiMo/APAT-1, (d) NiMo/APAT-2, (e) NiMo/APAT-3, (f) NiMo/APAT-4, (g) NiMo/AAT.

Table 6. HDS efficiency of the corresponding catalysts.

Catalyst	Support Additives Si/Al	S in Product (mg L^{-1})	HDS Efficiency (%)
NiMo/γ-Al_2O_3	-	56.9	94.4
NiMo/AST	-	51.1	95.0
NiMo/APAT-1	67	46.1	95.5
NiMo/APAT-2	33	36.8	96.4
NiMo/APAT-3	17	30.5	97.0
NiMo/APAT-4	9	35.6	96.5
NiMo/AAT	30	34.5	96.6

HDS Reactions at lower conversion also be repeated, and the details can be seen in Figures S2 and S3 in the part of Supplementary Information.

3. Discussion

To further investigate the effects of properties on their HDS performances for FCC diesel, systematic research on the correlation of HDS efficiencies with the synergistic effects of textural properties, acidity, MSI and morphology of the sulfided active metal species was discussed.

Generally, catalytic performances are closely concerned with the textural characteristics of catalysts. The addition of mesoporous support additives improves the overall pore structure of the support system of the catalyst. From Table 6, it can be found that the catalyst of NiMo/APAT-3 has a higher surface area, at around 225.6 m^2 g^{-1}, and a higher volume, at around 0.40 cm^3 g^{-1}, than catalysts of NiMo/γ-Al_2O_3 (167.4 m^2 g^{-1}, 0.34 m^2 g^{-1}) and NiMo/APAT-4 (224.2 m^2 g^{-1}, 0.39 m^2 g^{-1}). As is known to all, high surface area is proper for good distribution of active phases, while large pore diameter facilitates the elimination of diffusion resistance.

Acidity property is another important factor for HDS performance. Although the catalyst NiMo/AST has better textural properties than the series catalysts NiMo/APAT-x, it still has inferior HDS efficiency to that of the latter due to the lower number of acid sites. The incorporation of Al species into the PAT material and the obtained materials used as support additives could modulate the acid property of silica. According to FT-IR results (in Table 3), the material PAT-3 has the highest total number of weak sites (79.3 μmol g^{-1}), medium and strong sites (38.6 μmol g^{-1}); moreover, the highest number of B acid sites. The presence of L acid sites facilitates the hydrogenation reaction; in the meantime, B acid sites favor C-S and C-C bond cleavage [2], which are very important for the hydrodesulfurization reaction. Moreover, acidity accelerates the dealkylation and isomerization reactions, transforming the refractory sulfur reactants into more reactive components and consequently improving the HDS efficiency [54]. Thus, the catalyst NiMo/APAT-3 has outstanding HDS activity compared to the remaining catalysts.

Aside from the aforementioned factors, moderate MSI and the morphology of the active phases over the catalysts can also influence the HDS efficiency. The implanting of Al elements into the Si-TUD-1 material adjusts the active metal distributions and modifies the MSI, consistent with H_2-TPR analysis. H_2-TPR profiles indicate that the catalyst NiMo/APAT-3 has two lower reduction peaks (at 722 and 1069 K), compared to catalyst NiMo/γ-Al_2O_3 (at 750 and 1142 K), which suggests that the PAT material support additive possesses a lower MSI derived from the siliceous framework of TUD-1, and leads to the generation of Mo species in octahedral coordination, the precursors to forming more "type II" phases with brim and edge sites responsible for hydrodesulfurization.

The strong MSI over the sulfided catalyst NiMo/γ-Al_2O_3 results in the long length (3.9 nm) and low stack number (1.6) of the MoS_2 slabs, facilitating the formation of more "type I" active phases that possess fewer brim and edge active sites, and therefore contribute to a lower activity. The catalyst NiMo/APAT-3 exhibits relatively short lengths (3.2 nm) and suitable layer number (2.5) of the MoS_2 slabs, indicating most active sites existed as "type II", which are essential for S removal by perpendicular adsorption through the sulfur atom of the reactant molecules [51,55]. Moreover, the f_{Mo} parameter of the catalyst NiMo/APAT-3 (0.31) is significantly higher than that of catalyst NiMo/γ-Al_2O_3 (0.26), confirming that the catalyst NiMo/APAT-3 possesses more active edge Mo atoms than the latter. The catalyst NiMo/AAT with the support additive of Al-TUD-1 has a similar high f_{Mo} parameter (0.32) to the catalyst NiMo/APAT-3, while having a higher layer number (2.8). The high layer number of the MoS_2 slabs leads to the decrease of the total amount of accessible sites, since only the top layer of multi-stacks can be exposed to the brim sites [56]. These theoretical explanations are suggested to be the underlying reasons for the HDS activity order: NiMo/APAT-3 > NiMo/AAT > NiMo/γ-Al_2O_3.

The research synthesized Al-modified TUD-1 materials through the post-synthesis method, which possessed appropriate textural properties and suitable acidity, and the PAT material support additive facilitated to the lower MSI in the catalyst. Therefore, NiMo/APAT-3 exhibited the highest HDS efficiency, which would be a promising catalyst for the industrial hydrotreating technique.

4. Materials and Methods

4.1. Materials

Siliceous TUD-1 mesoporous material was produced following the procedure publicized by Jansen et al. [21] by one-pot sol-gel technique. Typically, a mixture of TEA (≥98%, Sinopharm Chemical Reagent, Co., Ltd (SCRC), shanghai, China) and water was added drop-wise to a certain amount of tetraethyl orthosilicate (TEOS) under vigorous stirring. Subsequently, a controlled number of TEAOH (25 wt %) was dropped into the above mixture. A clear gel was obtained having a molar ratio composition of SiO_2:1TEA:0.2TEAOH:11H_2O. After stirring for some minutes, the final mixture was aged for 24 h, and then dried at 373 K, followed by a hydrothermal treatment at 453 K for 6 h, finally calcined at 873 K for 10 h with a ramp of 274 K/min. After the above steps, purely Siliceous TUD-1 was obtained.

The siliceous TUD-1 was adopted as a parent material to prepare Al incorporation TUD-1 by post-synthesis method [37]. Various amounts of aluminum isopropoxide (≥98%, SCRC) were initially dissolved in isopropanol, then the obtained Siliceous TUD-1 was added to the above mixture under stirring for 3–5 h. After suction filtration and washing with dry isopropoxide, the solid compound was finally calcined at 823 K for 6 h. For the sake of expression, the alkoxide addition amounts were represented by Al_2O_3 percentage, then the synthesized materials were named as PAT-x, where PAT represents post-synthesis aluminum modified TUD-1 and x represents the weight ratio of Al_2O_3, x = 1, 2, 3 and 4, corresponding to Al_2O_3 percentages of 3%, 6%, 12% and 18%, respectively.

Aluminum in-situ modified TUD-1 noted as Al-TUD-1 was synthesized via the conventional direct synthesis method described in the literature [38] with a Si/Al value of 30.

4.2. Production of Supports and Catalysts

The supports of each catalyst were made up of 70 wt % commercial γ-Al_2O_3 and 30 wt % different support additives such as Siliceous TUD-1, Al-TUD-1 or PAT-x material through the mechanical grinding method. The corresponding catalysts were produced via a two-step incipient impregnation technique using ammonium heptamolybdate as Mo source and nickel nitrate as Ni source. After each step, the as-prepared samples were dispersed by a sonic bath for 30 min. The final samples were calcined at 823 K for 4 h after dried at 383 K for 4 h.

All catalysts have the same active metal contents (MoO_3 15.5 wt % and NiO 3.5 wt %) and support proportion (81 wt %).

Furthermore, the catalysts were designated as NiMo/γ-Al_2O_3-Si-TUD-1 (NiMo/AST), NiMo/γ-Al_2O_3-Al-TUD-1 (NiMo/AAT), NiMo/γ-Al_2O_3-PAT-1 (NiMo/APAT-1), NiMo/γ-Al_2O_3-PAT-2 (NiMo/APAT-2), NiMo/γ-Al_2O_3-PAT-3 (NiMo/APAT-3) and NiMo/γ-Al_2O_3-PAT-4 (NiMo/APAT-4). The traditional NiMo/γ-Al_2O_3 catalyst was used as the reference.

4.3. Characterization of Supports and Catalysts

The supports and catalysts were analyzed using N_2 adsorption-desorption, XRD, ICP, SEM, Py-IR, ^{27}Al MAS NMR, UV-vis, H_2-TPR and HRTEM.

N_2 adsorption-desorption were performed at 77 K on instrument of a Micromeritics TriStar II 2020 porosimetry analyzer. Prior to each measurement, about 0.2 g samples were degassed at 623 K for 4 h under high vacuum. The surface area was via the BET method. The pore size was via the BJH method.

XRD patterns were measured on an instrument of Shimadzu X-6000 using Cu Kα radiation operated at a ray tube voltage of 40 kV, small angle range: 2θ of 0.7°~10°, bighorn range: 2θ of 10°~90°.

The SEM images of the catalysts were characterized on a Quanta 200 F instruments, combined with a Tecnai F20 electron microscopy for the EDS elemental mapping technology.

^{27}Al MAS NMR were analyzed on a Bruker MSL-300NMR spectrometer.

The UV-vis diffuse reflectance spectra were measured on a Hitachi U-4100 spectrophotomer equipped with an integration sphere diffuse reflectance attachment.

The Py-IR experiments were operated on a MAGNAIR 560 FTIR instrument.

H_2-TPR analysis was tested using a Quantachrome apparatus (Autosorb-iQ, USA).

HRTEM of the supported catalysts were characterized on a Philips Tecnai G2 F20 transmission electron.

4.4. Catalytic Activity Measurement

The HDS activity were evaluated in a fixed bed reactor using FCC diesel as feedstock from PetroChina Hohhot petrochemical company, with S content and N content are 1013.8 mg/L and 640.3 mg/L respectively.

Prior to the test of catalytic performance, 2 g catalyst with a diameter of 40–60 mesh was presulfided by 2 wt % CS_2-cyclohexane and H_2/cyclohexane ratio of 600 for 4 h under the conditions of 593 K and 4 MPa.

After presulfidation, the HDS performances were evaluated at the temperature of 623 K, meanwhile the pressure of 5.0 MPa, H_2 to Oil ratio of 600 and weight hourly space velocity (WHSV) of 1.0 h^{-1}. The final product sample was collected at steady state after 9 h on stream, and each evaluation experiment has been made three times in parallel, and taken the average to calculate the catalytic hydrodesulfurization efficiency. The S amounts were obtained by using a RPP-2000SN sulfur detector. The measurement deviation is within 2 mg/L. The final HDS efficiency of each catalyst is the average value of these 3 samples.

The HDS efficiency is obtained by the Equation (3).

$$\text{HDS efficiency} = (S_f - S_p)/S_f \quad (3)$$

where S_f refers to the amount of sulfur in feed, and S_p refers to the sulfur in product.

5. Conclusions

Siliceous TUD-1 mesoporous material was prepared by one-pot sol-gel technique. Then PAT materials with different Al contents adopting aluminum isopropoxide to be the Al sources in organic solvents were prepared through the post-synthesis method. The as-synthesized supports and the corresponding NiMo catalysts were analyzed using XRD, N_2-adsorption, SEM, Py-IR, ^{27}Al MAS NMR, UV-vis, H_2-TPR ICP and HRTEM methods. The characterizations of XRD and N_2-adsorption showed that the post-synthesis Al grafting process had no significant influence on the pore structure of Si-TUD-1. Furthermore, the results of Py-IR and ^{27}Al MAS NMR indicated that the addition of Al species could bring Lewis and B acid sites into Si-TUD-1 material, and the material of PAT-3 with suitable amounts of Al content had the highest total acidity sites and B acid sites. The supports of each catalyst were the mechanical mixture of the series PAT materials and the commercial γ-Al_2O_3. The corresponding catalysts were prepared with Ni and Mo as the active metals. The catalysts of NiMo/γ-Al_2O_3 and NiMo/AAT were prepared as well, and were used as the reference. The H_2-TPR results showed that the addition of PAT materials into the support system could result in the lower reduction peaks, and led to the generation of octahedral Mo elements with the easier redox and presulfurization properties. The HRTEM analysis exhibited that the sulfided catalyst NiMo/APAT-3 had a relatively short length (3.2 nm) and suitable stack (2.5) of the MoS_2 slabs.

The HDS efficiencies of all the supported catalysts were also evaluated with FCC diesel as feedstock. The catalytic results confirmed that the catalyst NiMo/APAT-3 possessed the highest HDS efficiency (97.0%), which could be associated with the synergistic effects of the appreciate textural characteristics, higher acidity, moderate MSI, relatively short length and suitable stacking of the MoS_2 slabs.

Supplementary Materials: The following are available online at www.mdpi.com/2073-4344/7/5/141/s1. Figure S1: Elemental mapping analysis of PAT materials (a) PAT-3; (b) PAT-4. Figure S2: The influence of different

WHSV to HDS efficiency over NiMo/APAT-3 catalyst. Figure S3: The lower conversion of the corresponding catalysts at a larger WHSV condition.

Acknowledgments: This work was financially supported by CNOOC project (CNOOC-KJ 135 FZDXM 00 LH 003 LH-2016), the National Natural Science Foundation of China (No. 21676298, U1463207 and 21503152), Opening Project of Guangxi Key Laboratory of Petrochemical Resource Processing and Process Intensification Technology (2015K003), CNPC Key Research Project and KLGCP (GCP201401).

Author Contributions: Zesheng Xia, Jianye Fu and Aijun Duan conceived and designed the experiments; Zesheng Xia and Jianye Fu performed the experiments; Zesheng Xia, Bo Wang and Qian Meng analyzed the data; Longnian Han, Huadong Wu and Dong Wang contributed reagents/materials/analysis tools; Zesheng Xia wrote the paper; Aijun Duan, Zhen Zhao and Chunming Xu participated in research discussion.

Conflicts of Interest: The authors declare no conflict of interest.

Abbreviations

The following abbreviations have been used in this manuscript:

PAT	post synthesis aluminum modified TUD-1
Al-TUD-1	aluminum in-situ modified TUD-1
HDS	hydrodesulfurization
DBT	dibenzothiophene
4,6-DMDBT	4,6-dimethyldibenzothiophene
ALPOs	aluminiumphosphate
TEA	triethanolamine
TEAOH	tetraethyl ammonium hydroxide
TEOS	tetraethyl orthosilicate
XRD	X-ray diffraction
SEM	scanning electron microscopy
UV-Vis	Ultraviolet-visible spectroscopy diffuse reflection spectrum
Py-IR	pyridine adsorption fourier-transform infrared
H_2-TPR	H_2 temperature-programmed reduction
HRTEM	High-resolution transmission electron microscopy methods
BET	Brunauer-Emmett-Teller
BJH	Barrett-Joyner-Halenda
EDX	energy-dispersive X-ray spectrometer
IUPAC	International Union of Pure and Applied Chemistry
MSI	metal-support interaction
^{27}Al MAS NMR	^{27}Al solid-state magic-angle-spinning nuclear magnetic resonance
WHSV	weight hourly space velocity
NiMo/AST	NiMo/γ-Al_2O_3-Si-TUD-1
NiMo/AAT	NiMo/γ-Al_2O_3-Al-TUD-1
NiMo/APAT-1	NiMo/γ-Al_2O_3-PAT-1
NiMo/APAT-2	NiMo/γ-Al_2O_3-PAT-2
NiMo/APAT-3	NiMo/γ-Al_2O_3-PAT-3
NiMo/APAT-4	NiMo/γ-Al_2O_3-PAT-4
S_f	sulfur concentrations in feed
S_p	sulfur concentrations in product
f_{Mo}	the fraction of Mo atoms located on the edges of MoS_2 clusters, was calculated using the ratio of Mo_{edge}/Mo_{total}
Mo_{edge}	the numbers of Mo atoms located on the edges of MoS_2 particles
Mo_{total}	the total amount of Mo atoms
n_i	the number of Mo atoms along one side of a MoS_2 slab determined from its length (L = 3.2 ($2n_i - 1$) Å)
t	the total number of the layers about 400 slabs obtained in 25 pieces of HRTEM micrographs
x_i	the number of slabs or stacks in a given range of length or stacking layer number
M_i	the slab length or the stacking layer number of a stacked MoS_2 unit

References

1. Pawelec, B.; Navarro, R.; Camposmartin, J. Towards near zero-sulfur liquid fuels: A perspective review. *Catal. Sci. Technol.* **2011**, *1*, 23–42. [CrossRef]

2. Duan, A.; Li, T.; Zhen, Z. Synthesis of hierarchically porous L-KIT-6 silica-alumina material and the super catalytic performances for hydrodesulfurization of benzothiophene. *Appl. Catal. B Environ.* **2015**, *165*, 763–773. [CrossRef]
3. Li, T.; Duan, A.; Zhen, Z. Synthesis of ordered hierarchically porous L-SBA-15 material and its hydro-upgrading performance for FCC gasoline. *Fuel* **2014**, *117*, 974–980. [CrossRef]
4. Luan, Z.; Hartmann, M.; Zhao, D. Alumination and ion exchange of mesoporous SBA-15 molecular sieves. *Chem. Mater.* **1999**, *11*, 1621–1627. [CrossRef]
5. Han, Y.; Xiao, F.S.; Wu, S. A novel method for incorporation of heteroatoms into the framework of ordered mesoporous silica materials synthesized in strong acidic media. *J. Phys. Chem. B* **2001**, *105*, 7963–7966. [CrossRef]
6. Morey, M.S.; O'Brien, S.; Schwarz, S. Hydrothermal and postsynthesis surface modification of cubic, MCM-48, and ultralarge pore SBA-15 mesoporous silica with titanium. *Chem. Mater.* **2000**, *12*, 898–911. [CrossRef]
7. Luan, Z.; Bae, J.Y.; Kevan, L. Vanadosilicate mesoporous SBA-15 molecular sieves incorporated with N-alkylphenothiazines. *Chem. Mater.* **2000**, *12*, 3202–3207. [CrossRef]
8. Yue, Y.H.; Gédéon, A.; Bonardet, J.L. Direct incorporation of A1 in SBA mesoporous materials: Characterization, stability and catalytic activity. *Stud. Surf. Sci. Catal.* **2000**, *129*, 209–218.
9. Newalkar, B.L.; Johnson Olanrewaju, A.; Komarneni, S. Microwave-hydrothermal synthesis and characterization of zirconium substituted SBA-15 mesoporous Silica. *J. Phys. Chem. B* **2001**, *105*, 8356–8360. [CrossRef]
10. Ryoo, R.; Mi, J.K. Generalised route to the preparation of mesoporous metallo-silicates via post-synthetic metal implantation. *Chem. Commun.* **1997**, *93*, 2225–2226. [CrossRef]
11. Mokaya, R. Post-synthesis grafting of Al onto MCM-41. *Chem. Commun.* **1997**, *22*, 2185–2186. [CrossRef]
12. Hamdan, H.; Endud, S.; He, H. Alumination of the purely siliceous mesoporous molecular sieve MCM-41 and its hydrothermal conversion into zeolite Na-A. *J. Cheminform.* **1996**, *92*, 2311–2315. [CrossRef]
13. Luca, V.; Maclachlan, D.J.; Bramley, R. Electron paramagnetic resonance and electron spin echo modulation study of surface sites of the porous aluminosilicate MCM-41 using transition metal ion probes. *J. Phys. Chem.* **1996**, *100*, 1793–1800. [CrossRef]
14. Suresh, C.; Santhanaraj, D.; Gurulakshmi, M. Mo-Ni/Al-SBA-15 (sulfide) catalysts for hydrodenitrogenation: Effect of Si/Al ratio on catalytic activity. *ACS Catal.* **2012**, *2*, 127–134. [CrossRef]
15. Zárate, D.O.D.; Fernández, L.; Beltrán, A. Expanding the atrane route: Generalized surfactant-free synthesis of mesoporous nanoparticulated xerogels. *Solid State Sci.* **2008**, *10*, 587–601. [CrossRef]
16. Liu, G.; Jia, M.; Zhou, Z. Synthesis of amorphous mesoporous aluminophosphate materials with high thermal stability using a citric acid route. *Chem. Commun.* **2004**, *10*, 1660–1661. [CrossRef] [PubMed]
17. Zheng, J.Y.; Pang, J.B.; Qiu, K.Y. Synthesis of mesoporous titanium dioxide materials by using a mixture of organic compounds as a non-surfactant template. *J. Phys. Chem.* **2001**, *11*, 3367–3372.
18. Liu, X.; Wei, Y.; Jin, D. Synthesis of mesoporous aluminum oxide with aluminum alkoxide and tartaric acid. *Mater. Lett.* **2000**, *42*, 143–149. [CrossRef]
19. Liu, Q.; Wang, A.; Wang, X. Mesoporous gamma-alumina synthesized by hydro-carboxylic acid as structure-directing agent. *Microporous Mesoporous Mater.* **2006**, *92*, 10–21. [CrossRef]
20. Liu, C.; Lambert, J.B.; Fu, L. Simple surfactant-free route to mesoporous organic-inorganic hybrid silicas containing covalently bound cyclodextrins. *J. Org. Chem.* **2004**, *69*, 2213–2216. [CrossRef] [PubMed]
21. Jansen, J.C.; Shan, Z.; Maschmeyer, T. A new templating method for three-dimensional mesopore networks. *Chem. Commun.* **2001**, *8*, 713–714. [CrossRef]
22. Angevine, P.J. Advanced catalytic materials for the refining and petrochemical industry: TUD-1. *ACS Symp.* **2008**, *1000*, 335–363.
23. Telalović, S.; Ramanathan, A.; Mul, G. TUD-1: Synthesis and application of a versatile catalyst, carrier, material. *New J. Chem.* **2010**, *20*, 642–658. [CrossRef] [PubMed]
24. Pachamuthu, M.P.; Srinivasan, V.V.; Maheswari, R. Lewis acidic ZrTUD-1 as catalyst for tert-butylation of phenol. *Appl. Catal. A Gen.* **2013**, *462*, 143–149. [CrossRef]
25. Sing, K.; Everett, D.; Hauk, R. Reporting physisorption data for gas/solid systems with special reference to the determination of surface-area and porosity. *Pure Appl. Chem.* **2009**, *57*, 603–619. [CrossRef]

26. Groen, J.C.; Peffer, L.A. A.; Pérez-RamíRez, J. Pore size determination in modified micro- and mesoporous materials. Pitfalls and limitations in gas adsorption data analysis. *Microporous Mesoporous Mater.* **2003**, *60*, 1–17. [CrossRef]
27. Rouquerol, J.; Avnir, D.; Everett, D.H. Guidelines for the characterization of porous solids. *Pure Appl. Chem.* **2001**, *87*, 1–9.
28. Janssen, A.H.; Yang, C.M.; Wang, Y. Localization of small metal (oxide) particles in SBA-15 using bright-field electron tomography. *J. Phys. Chem. B* **2003**, *107*, 10552–10556. [CrossRef]
29. Hamdy, M.S. One-step synthesis of M-doped TiO_2, nanoparticles in TUD-1 (M-TiO_2-TUD-1, M = Cr or V) and their photocatalytic performance under visible light irradiation. *J. Mol. Catal. A Chem.* **2014**, *393*, 39–46. [CrossRef]
30. Barzetti, T.; Selli, E.; Moscotti, D. Pyridine and ammonia as probes for FTIR analysis of solid acid catalysts. *J. Chem. Soc. Faraday Trans.* **1996**, *92*, 1401–1407. [CrossRef]
31. Zhang, X.; Wang, J.; Zhong, J. Characterization and catalytic performance of SAPO-11/Hβ composite molecular sieve compared with the mechanical mixture. *Microporous Mesoporous Mater.* **2008**, *108*, 13–21. [CrossRef]
32. Handjani, S.; Dzwigaj, S.; Blanchard, J. Comparing Al-SBA-15 support and Pt/Al-SBA-15 catalyst: Changes in Al speciation and acidic properties induced by the introduction of Pt via aqueous medium. *Top. Catal.* **2009**, *52*, 334–343. [CrossRef]
33. Witte, B.M.D.; Grobet, P.J.; Uytterhoeven, J.B. Pentacoordinated aluminum in noncalcined amorphous aluminosilicates, prepared in alkaline and acid mediums. *J. Phys. Chem.* **1995**, *99*, 6961–6965. [CrossRef]
34. Amir, G.; Miron, V.L.; Shimon, V. Characterization of aluminum species in alumina multilayer grafted MCM-41 using ^{27}Al FAM(II)-MQMAS NMR. *J. Phys. Chem. B* **2003**, *107*, 724–731.
35. Góra-Marek, K.; Derewiński, M.; Sarv, P. IR and NMR studies of mesoporous alumina and related aluminosilicates. *Catal. Today* **2005**, *101*, 131–138. [CrossRef]
36. Rochefoucauld, E.D.L.; Carrier, X.; Krafft, J.M. Mesoporous alumina of controlled pore size obtained by surface alumination of pure silica SBA-15. *Stud. Surf. Sci. Catal.* **2006**, *162*, 13–20.
37. Baca, M.; Rochefoucauld, E.D.L.; Ambroise, E. Characterization of mesoporous alumina prepared by surface alumination of SBA-15. *Microporous Mesoporous Mater.* **2008**, *110*, 232–241. [CrossRef]
38. Wang, Z.; Fu, J.; Deng, Y. Synthesis of aluminum-modified 3D mesoporous TUD-1 materials and their hydrotreating performance of FCC diesel. *RSC Adv.* **2015**, *5*, 5221–5230. [CrossRef]
39. Fu, J.; Zheng, P.; Du, P. Zirconium modified TUD-1 mesoporous catalysts for the hydrodesulfurization of FCC diesel. *Appl. Catal. A Gen.* **2015**, *502*, 320–328. [CrossRef]
40. Prins, R.; Ertl, G.; Knözinger, H.; Weitkam, J. *Handbook of Heterogeneous Catalysis*; Wiley-VCH: Weinheim, Germany, 1997; p. 1908.
41. Klimova, T.; Peña, L.; Lizama, L. Modification of activity and selectivity of NiMo/SBA-15 HDS catalysts by grafting of different metal oxides on the support surface. *Ind. Eng. Chem. Res.* **2008**, *48*, 1126–1133. [CrossRef]
42. Lizama, L.; Klimova, T. Highly active deep HDS catalysts prepared using Mo and W heteropolyacids supported on SBA-15. *Appl. Catal. B Environ.* **2008**, *82*, 139–150. [CrossRef]
43. Xiong, G.; Feng, Z.; Li, J. UV Resonance raman spectroscopic studies on the genesis of highly dispersed surface molybdate species on γ-Alumina. *J. Phys. Chem. B* **2000**, *104*, 3581–3588. [CrossRef]
44. Gao, D.; Duan, A.; Xin, Z. Synthesis of NiMo catalysts supported on mesoporous Al-SBA-15 with different morphologies and their catalytic performance of DBT HDS. *Appl. Catal. B Environ.* **2015**, *165*, 269–284. [CrossRef]
45. Topsøe, H.; Clausen, B.S.; Candia, R. In situ Mössbauer emission spectroscopy studies of unsupported and supported sulfided CoMo hydrodesulfurization catalysts: Evidence for and nature of a CoMoS phase. *J. Catal.* **1981**, *68*, 433–452. [CrossRef]
46. Damyanova, S.; Spojakina, A.; Jiratova, K. Effect of mixed titania-alumina supports on the phase composition of NiMo/TiO_2-Al_2O_3 catalysts. *Appl. Catal. A Gen.* **1995**, *125*, 257–269. [CrossRef]
47. Cordero, R.L.; Agudo, A.L. Effect of water extraction on the surface properties of Mo/Al_2O_3 and NiMo/Al_2O_3 hydrotreating catalysts. *Appl. Catal. A Gen.* **2000**, *202*, 23–35. [CrossRef]
48. Rodriguez, J.A.; Kim, J.Y.; Hanson, J.C. Reduction of $CoMoO_4$ and $NiMoO_4$: In situ time-resolved XRD Studies. *Catal. Lett.* **2002**, *82*, 103–109. [CrossRef]
49. Fan, Y.; Xiao, H.; Shi, G. Citric acid-assisted hydrothermal method for preparing NiW/USY-Al_2O_3 ultradeep hydrodesulfurization catalysts. *J. Catal.* **2011**, *279*, 27–35. [CrossRef]

50. Kasztelan, S.; Toulhoat, H.; Grimblot, J. A geometrical model of the active phase of hydrotreating catalysts. *Appl. Catal.* **1984**, *13*, 127–159. [CrossRef]
51. Gutiérrez, O.Y.; Klimova, T. Effect of the support on the high activity of the (Ni)Mo/ZrO_2-SBA-15 catalyst in the simultaneous hydrodesulfurization of DBT and 4,6-DMDBT. *J. Catal.* **2011**, *281*, 50–62. [CrossRef]
52. Topsøe, H. The role of Co-Mo-S type structures in hydrotreating catalysts. *Appl. Catal. A Gen.* **2007**, *322*, 3–8. [CrossRef]
53. Han, W.; Yuan, P.; Fan, Y. Synthesis, self-assembly and disassembly of mono-dispersed Mo-based inorganic-organic hybrid nanocrystals. *J. Mater. Chem.* **2012**, *22*, 12121–12127. [CrossRef]
54. Pérot, G. Hydrotreating catalysts containing zeolites and related materials-mechanistic aspects related to deep desulfurization. *Catal. Today* **2003**, *86*, 111–128. [CrossRef]
55. Landau, M.V.; Vradman, L.; Herskowitz, M. Ultrasonically controlled deposition—Precipitation: Co-Mo HDS catalysts deposited on wide-pore MCM material. *J. Catal.* **2001**, *201*, 22–36. [CrossRef]
56. Song, C. An overview of new approaches to deep desulfurization for ultra-clean gasoline, diesel fuel and jet fuel. *Catal. Today* **2003**, *86*, 211–263. [CrossRef]